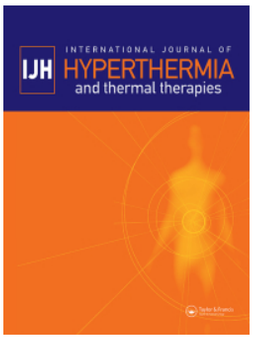

International Journal of Hyperthermia

ISSN: 0265-6736 (Print) 1464-5157 (Online) Journal homepage: informahealthcare.com/journals/ihyt20

# Absolute temperature imaging using intermolecular multiple quantum MRI

Elizabeth R. Jenista, Rosa T. Branca & Warren S. Warren

**To cite this article:** Elizabeth R. Jenista, Rosa T. Branca & Warren S. Warren (2010) Absolute temperature imaging using intermolecular multiple quantum MRI, International Journal of Hyperthermia, 26:7, 725-734, DOI: 10.3109/02656736.2010.499527

**To link to this article:** https://doi.org/10.3109/02656736.2010.499527

*Int. J. Hyperthermia*, October 2010; 26(7): 725–734

informa
healthcare

**REVIEW ARTICLE**

# Absolute temperature imaging using intermolecular multiple quantum MRI

ELIZABETH R. JENISTA, ROSA T. BRANCA, & WARREN S. WARREN

*Department of Chemistry, Duke University, Durham, North Carolina, USA*

*(Received 1 February 2010; Revised 4 June 2010; Accepted 5 June 2010)*

**Abstract**

*Purpose:* A review of MRI temperature imaging methods based on intermolecular multiple quantum coherences (iMQCs) is presented. Temperature imaging based on iMQCs can provide absolute temperature maps that circumvent the artefacts that other proton frequency shift techniques suffer from such as distortions to the detected temperature due to susceptibility changes and magnetic field inhomogeneities. Thermometry based on iMQCs is promising in high-fat tissues such as the breast, since it relies on the fat signal as an internal reference. This review covers the theoretical background of iMQCs, and the necessary adaptations for temperature imaging using iMQCs.

*Materials and methods:* Data is presented from several papers on iMQC temperature imaging. These studies were done at 7T in both phantoms and in vivo. Results from phantoms of cream (homogeneous mixture of water and fat) are presented as well as in vivo temperature maps in obese mice.

*Results:* Thermometry based on iMQCs offers the potential to provide temperature maps which are free of artefacts due to susceptibility and magnetic field inhomogeneities, and detect temperature on an absolute scale.

*Conclusions:* The data presented in the papers reviewed highlights the promise of iMQC-based temperature imaging in fatty tissues such as the breast. The change in susceptibility of fat with temperature makes standard proton frequency shift methods (even with fat suppression) challenging and iMQC-based imaging offers an alternative approach.

**Keywords:** *CRAZED, intermolecular multiple quantum coherences, magnetic resonance temperature imaging, proton resonance frequency shift, thermometry*

## Introduction

Numerous studies have shown that combining hyperthermic therapy with radiotherapy can result in a wide variety of benefits including increased tumour response and increased survival rates [1–3]. However, hyperthermic therapy requires the accurate delivery of a prescribed temperature dose for a sustained time (usually 40°–45°C over 30–90 min for thermal therapy, or temperatures greater than 45°C for thermal ablation [4]) and monitoring the heating is challenging [5, 6]. Extensive, invasive thermometry usually done via multiple thermocouples can be used, and several studies have invasively monitored temperature during treatment and found the outcome of the treatment is directly tied to the temperature achieved [7–13]. Recently, a pilot study combining neoadjuvant liposomal doxorubicin, paclitaxel and hyperthermia was conducted on locally advanced breast cancer [14] with encouraging results. In that study, temperature was monitored by a thermocouple, and the pathological outcome was related to the thermal dose. MRI can monitor temperature non-invasively and without the use of ionising radiation [15–23]. The most commonly used temperature-sensitive MR parameter is the change in the chemical shift of water with

Correspondence: Elizabeth R. Jenista, 124 Science Drive, 2220 FFSC, Box 90347, Durham, NC 27708, USA. Tel: 919-660-8459. E-mail: elizabeth.specht@duke.edu

ISSN 0265–6736 print/ISSN 1464–5157 online 
DOI: 10.3109/02656736.2010.499527

temperature. The temperature sensitivity of the water chemical shift was first observed by Hindman in 1966 [24] and was later adapted to temperature imaging by Ishiara [21] and De Poorter [18, 19]. In magnetic resonance the resonance frequency of a particular spin is defined as [25]:

$$\omega = (1 - \sigma(T))\gamma B_0 \quad (1)$$

The chemical shift determined by the local electronic environment is $\sigma$, $\gamma$ is the gyromagnetic ratio (42.8 MHz/T for protons) and $B_0$ is the main magnetic field. The chemical shift is determined by the local electron environment. During heating the electronic environment of the water spins changes because of changes in the hydrogen bonding network. These changes cause a shift in the proton resonance frequency of about 0.01 ppm/°C. This effect is often referred to as the proton resonance frequency (PRF) shift, but it is important to realise that non-water protons are not shifted by the same amount, as discussed below.

For lean tissues such as muscle, the temperature dependence of the water chemical shift is well known and fairly constant across tissue types [26]. However, the magnetic susceptibility, or magnetic flux density, can also change with temperature [27], adding an additional complication to the PRF methods. The observed frequency of a spin depends both on the local magnetic field, as well as the chemical shift, so changes to the local magnetic field due to susceptibility changes also change the resonance frequency [27–29]. The local magnetic field can be approximated as [18]:

$$\omega = (1 - \sigma(T))\gamma B_{\text{local}}$$
$$B_{\text{local}} \cong \left(1 - \frac{2\chi(T)}{3} - \sigma(T)\right)B_{\text{mac}} \quad (2)$$

$B_{\text{local}}$ is the local magnetic field experienced by the nucleus (which includes both the static magnetic field, $B_{\text{mac}}$, as well as the local effects), $\chi$ is the temperature dependent susceptibility constant of the material and $\sigma(T)$ is the chemical shift (which depends on the chemical environment). $B_{\text{mac}}$ is the macroscopic magnetisation and is a function of the main magnetic field ($B_0$), the susceptibility distribution and sample geometry. The resonance frequency of water protons does not depend only on the chemical shift ($\sigma$) of the protons, but it is also affected by tissue magnetic susceptibility. The temperature dependence of $\chi$ depends on the tissue type and is 0.0026 ppm/°C for pure water, 0.0019 ppm/°C for muscle and 0.0094 ppm/°C in fat [18, 30]. In lean tissues the change in chemical shift dominates (at 0.01 ppm/°C), and the error from changes in susceptibility only creates 10% variations in the detected temperature [18].

In tissues with a high fat content, such as the breast, application of PRF methods is not immediately straightforward. We cannot monitor temperature changes by looking at the resonance frequency of fat spins, since the chemical shift of fat is nearly constant over the range of temperatures used in hyperthermic treatment (0.00018 ppm/°C) [31]. Thus, in tissues with large fat content, fat suppression methods are almost always used. More importantly, in fatty tissues the susceptibility changes are quite large. These changes are significant enough to affect the resonance frequency of the nearby water spins and seriously complicate the temperature measurements.

A temperature imaging technique using intermolecular multiple quantum coherences (iMQCs) has been developed to address the issues associated with temperature imaging in fatty tissues. The iMQC based technique (called HOT [32]) is designed for use in tissues with high fat content and is insensitive to errors due to changes in susceptibility of both water and fat, as well as magnetic field drift and magnetic field inhomogeneities. In addition, HOT also provides absolute temperature measurements instead of relative temperature measurements (as obtained from PRF methods). This review will focus on the underlying physics of iMQCs, the properties of iMQCs which make them uniquely suited for temperature detection in high fat content tissues and demonstrations of iMQC-based temperature imaging.

## Why iMQCs?

Intermolecular multiple quantum coherences (iMQCs) are a type of magnetic resonance signal which comes from the simultaneous transition of two spins on separate molecules [33–50]. The distance between the two molecules is tunable, but in common applications is about 100 μm. The two most common types of iMQCs are intermolecular zero quantum coherences (iZQCs) and intermolecular double quantum coherences (iDQCs). Both types of iMQCs are used in the HOT pulse sequence, and allow for the detection of absolute temperature using MRI.

The basic approach with the HOT sequence is to monitor the changes in the difference between the chemical shift of a water spin and a nearby fat spin. This removes the effects of magnetic field inhomogeneities, susceptibility gradients and magnetic field drift. While iMQC temperature imaging is superficially very similar to PRF methods, the physics of the signal isolates changes in the chemical shift of water, rather than its resonance frequency, thereby making temperature maps that circumvent most artefacts and

can be interpreted on an absolute scale. In addition, this method is less sensitive to physiological motion (such as respiratory motion) because the resonance frequency difference that this method detects is more likely to remain constant when both spins move.

A key feature of the HOT technique is that it is insensitive to changes in the bulk susceptibility of the tissue. In order to understand this, let us consider iZQCs in particular. As we will see in the next sections, an iZQC evolves at the difference frequency of the two spins. A mixed spin iZQC (one between a water spin and a fat spin) evolves at the difference in frequency between water and fat. At 7T, for example, this frequency is 1000 Hz. Let us consider the effect of a large susceptibility change. If the susceptibility changed by 10 ppm (an extreme example, much more than expected due to heating effects), this would cause a change in the proton resonance frequency of $300\,\mathrm{MHz} * 10 \times 10^{6} = 3000\,\mathrm{Hz}$, or a temperature misregistration of 1000°C. Now consider the effect of the same susceptibility gradient on the iZQC frequency. The iZQC transition occurs at the difference frequency of water and fat, so at 7T, this frequency is 1000 Hz. The effect of the 10 ppm susceptibility gradient would cause a change in the iZQC frequency of $1000 * 10 \times 10^{-6} = 0.01\,\mathrm{Hz}$, or a misregistration of temperature of 0.0033°C. The key thing to remember is that the HOT sequence isolates changes to $\sigma$, the chemical shift constant of water, and circumvents artefacts caused by changes to the susceptibility, magnetic field inhomogneities and drift.

## The theory of iMQCs

The HOT technique relies on detection of signals from intermolecular multiple-quantum coherences, which are unfamiliar to the medical community (and, indeed, to most people in the magnetic resonance community in general). To understand these effects, a bit of historical perspective is in order. Conventional MR contrast relies, for the most part, on spin physics which was well understood half a century ago: relaxation times of different magnetisation components ($T_1, T_2$), resonance frequency differences due to susceptibility changes ($T_2^*$) or chemical shifts, and diffusion. By the early 1990s, the mathematical framework behind both NMR and MRI was believed to be extremely well understood; in most cases, if one had a result that disagreed with the theoretical predictions, then the experiment, not the theory was at fault. However, at that time the underlying framework of magnetic resonance was challenged by a series of very simple pulse sequences which provided very unusual results [40]. For example, two 90° pulses and a gradient were applied to very simple samples (such as water, or chloroform and benzene), but resulted in a signal appearing where the theory predicted no signal should exist. Even stranger, that signal had many unique characteristics which led some researchers [37, 50] to question the underlying theory.

After some analysis, it became clear that several assumptions made in the underlying theory of magnetic resonance were not always true, and under certain experimental conditions, these assumptions needed to be revisited. The details of the assumptions and the necessary corrections to the theory of magnetic resonance are contained in the supplemental information. The bottom line is iMQCs, which are readily shown in the conventional treatment of magnetic resonance to be unobservable, can lead to large signals which are easily detected in spectroscopy and imaging. More importantly, signals from experiments such as CRAZED (see below) have intrinsic properties which differ from those seen in conventional magnetic resonance experiments, and which can reflect image information that is not readily extracted by other means.

## Description of the CRAZED sequence

The CRAZED sequence is the standard sequence used to detect iMQCs, and the HOT sequence is based upon the CRAZED sequence. In the CRAZED experiment, the first RF pulse excites standard single quantum coherences as well as the double and zero quantum coherences. Higher order multiple quantum coherences such as triple quantum coherences are also excited, but the signal intensity of these coherences is very small and imaging applications of these coherences is limited at clinically relevant fields [39]. Double quantum and zero quantum coherences can be visualised by drawing the energy level diagram for a 2-spin system (Figure 1B). Double quantum coherences correspond to simultaneous transitions of both spins in the same direction (a flip-flip transition or up-up to down-down). The net change in angular momentum is 2 (instead of 1 for a standard transition). A zero quantum coherence is the simultaneous transition of two spins in opposite directions (a flip-flop transition, or up-down to down-up). The net change in angular momentum is 0.

The energy (or frequency) for any transition is given by the difference in the energy levels, thus the frequency for a double quantum transition is the energy difference between the upper energy level and the lower one ($E_4 - E_1$). The energy of the uppermost level is given by $E_4 = \hbar(-1/2\omega_1 - 1/2\omega_2)$ and the lower energy level is $E_1 = \hbar(1/2\omega_1 + 1/2\omega_2)$, thus the energy of the transition comes at the sum of the

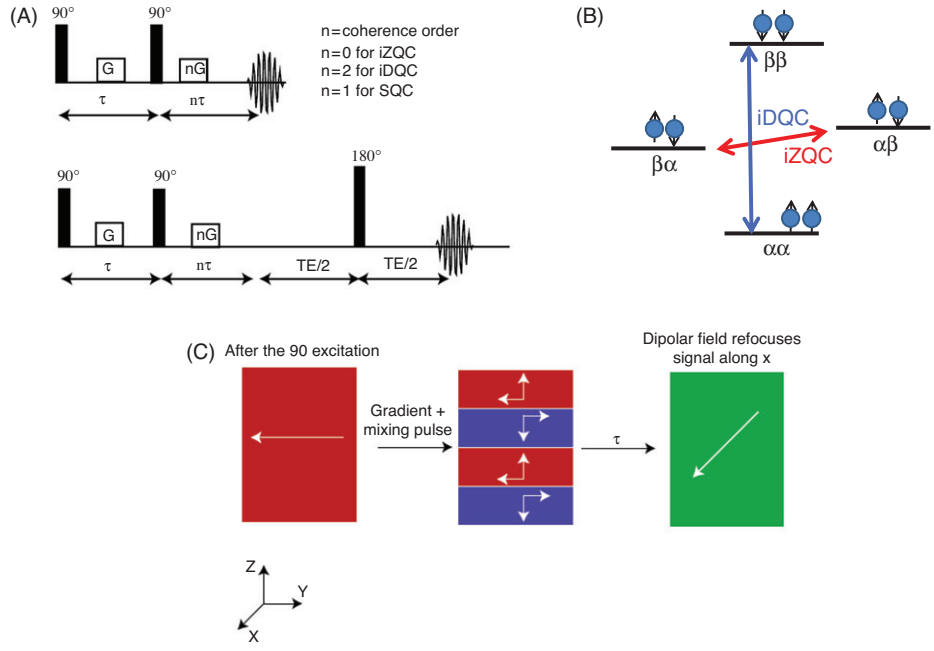


Figure 1. (A) Standard iMQC pulse sequence. The top pulse sequence shows the initial CRAZED sequence, while the bottom figure includes a spin echo detection to compensate for $T_2^*$ dephasing. (B) Energy level diagram for 2-spin system. The iMQC transitions are 2-spin transitions in which both spins flip in the same way ($\alpha\alpha$ to $\beta\beta$, or up-up to down-down) to create an iDQC, or in opposite directions ($\alpha\beta$ to $\beta\alpha$ or up-down to down-up) to create an iZQC. (C) Refocusing effect of the dipolar field created by the gradient and the mixing pulse on the dephased transverse magnetisation. The 90° pulse puts the magnetisation into the plane. The gradient spatially modulates the transverse magnetisation, and the mixing pulse tilts some portion of the modulated magnetisation back along the $z$-axis. The modulated longitudinal magnetisation interacts with the transverse magnetisation causing a signal refocusing at a later time.

two frequencies. Since a zero quantum transition is a transition between energy levels $E_2$ and $E_3$, the energy of that transition is $E_2 - E_3 = \hbar(\omega_1 - \omega_2)$.

After the initial pulse excites the multiple quantum coherences, a pair of magnetic field gradients and an additional RF pulse are applied to the sample. The effect of the gradients is complex since it acts on the system in two ways. First, it works as a coherence selection gradient. When the gradient is applied to the system it creates a spatial distribution of resonance frequencies which dephases the coherences excited by the first excitation pulse differently. A double quantum coherence will be dephased twice as much as a single quantum coherence, while a zero quantum coherence will not be affected at all. This is because in a double quantum coherence the effect of the gradient is on both the spins and adds up, while in a zero quantum coherence the effect is cancelled out.

The gradient also breaks the magnetic isotropy of the sample. When combined with the mixing pulse, the gradient re-introduces the dipolar field to the sample and converts the unobservable multiple quantum terms into observable single quantum terms. A more visual explanation of how this works is given in Figure 1C. After the application of the 90° pulse, all the magnetisation is pointed along one direction in the transverse plane. The gradient is applied, which winds the magnetisation into a helix along the direction of the gradient. The second pulse tips some of that magnetisation back along the $z$-axis. Depending on the phase of the magnetisation vector before the second pulse, the $z$-component of the magnetisation will be pointed either along $+z$ or $-z$. The $z$-magnetisation created by this second pulse exerts a force on the remaining magnetisation in the transverse plane causing it to refocus. The time that it takes for the magnetisation to refocus depends on the size of the magnetisation that was tipped along the $z$ axis, and this time is referred to as the 'dipolar demagnetising time'. The refocusing created by the gradient and the pulse is a qualitative description of the behaviour of the dipolar field and how it transforms the multiple quantum signal to observable signal.

## Methods

### *Modifications of the CRAZED sequence for temperature imaging: the HOT sequence*

Temperature detection with iMQCs requires the exclusive detection of mixed spin iMQCs in a

clinically reasonable amount of time (less than 2 min). This is accomplished by a modified CRAZED sequence called the HOT sequence. In a sample which is a mixture of two chemical species (for example, water and fat in tissue) there are 2 types of iMQC. There are the same spin iMQCs from pairs of water spins and pairs of fat spins. These coherences do not contain the necessary temperature information and are filtered out in the HOT sequence in order to detect clean iMQC temperature maps. The other kind of iMQCs is the mixed spin iMQCs between water and fat spins which is retained by the HOT sequence. The signal derived from these coherences is temperature dependent and is unaffected by magnetic field inhomogeneities and susceptibility changes.

Unlike the CRAZED sequence, which usually selects the signal from a particular coherence order, the HOT sequence uses a combination of iZQCs and iDQCs to get temperature maps. While it is intuitively clear that iZQCs retain chemical shift information while removing inhomogeneous broadening, +2-quantum iDQC evolution during one period (at the sum of the two different resonance frequencies) can combine with −1-quantum evolution during a later period to also give a signal that is free of inhomogeneous broadening [51]. The inhomogeneous broadening acquired during the time the coherence is +2 is twice the broadening that the coherence will experience when it is a −1-quantum coherence. If the timings are arranged so that the time as a −1 quantum coherence is twice as long as the time when it is a +2 coherence, then the inhomogeneous broadening will get reversed and iDQC signal can also be used to detect temperature.

An additional modification of the pulse sequence is necessary to enable rapid temperature measurements. In order to map out the temperature dependence of the iMQC signal, the evolution period ($\tau$) during which the coherences are iMQCs must be incremented so the temperature dependent phase shift can be extracted. This results in a lengthy imaging process which makes it unfavourable for dynamic temperature imaging. Many techniques have been developed to enable rapid acquisition of iMQC images [17, 52–58], such as techniques which include RARE or EPI acquisitions. RARE based accelerations of the sequence are unfavourable because of the potential issues with SAR, and EPI acquisitions impose an intolerable $T_2^*$ decay on the signal. In order to accelerate the acquisition of iMQC temperature maps, an alternative approach was used – one in which multiple acquisitions are acquired in each scan. Each acquisition has a different amount of evolution time allowing for rapid acquisitions of temperature maps.

Table I. Phase cycling for two-window HOT.

| Scan | 90 | $180_I$ | $90_S$ | Rcvr 1 | Rcvr 2 |
|---|---|---|---|---|---|
| 1 | 0 | 0 | 0 | 0 | 0 |
| 2 | 1 | 2 | 0 | 2 | 0 |
| 3 | 2 | 0 | 0 | 0 | 0 |
| 4 | 3 | 2 | 0 | 2 | 0 |

*Coherence pathways*

In order to rapidly acquire temperature maps using iMQCs, two acquisitions with different amounts of evolution are used. The different evolution in each acquisition window comes from the signal in each window experiencing a different coherence pathway. The phase cycling for the HOT sequence is given in Table I. The different coherence pathways also allow for robust filtering of the mixed spin iMQC signal. A product operator description of the exact details of the HOT sequence is provided in the supplemental information.

The first coherence pathway selects signals that were double quantum coherences during the first time period, $t_1$. During $t_1$, the iDQC signal evolves at the sum of the resonance frequencies of the two participating spins $(\omega_I + \omega_S) \star t_1$, where I and S represent the two different spin types. The selective inversion pulse (on the I spins) changes the sign of the I coherences, and the coherence is converted to an iZQC. During the subsequent time period, $\tau$, the signal evolves at the iZQC frequency $(\omega_S - \omega_I) \star \tau$. The selective mixing pulse on the S spins converts the two-spin iZQC coherence into a two-spin iSQC coherence, and dipolar couplings convert this into a detectable one-spin SQC. The signal evolves as an SQC for TE/2, then the refocusing pulse reverses the sign of this coherence and it evolves for a time of TE/2–$2t_1$, resulting in an evolution during this period of $-2\omega_I t_1$. The net evolution experienced by this signal is then $(\omega_S - \omega_I) \star (t_1 + \tau)$. The resulting signal essentially evolves as an iZQC for the time $t_1 + \tau$ allowing for clean, absolute temperature imaging.

The second coherence pathway, acquired in the second acquisition window, detects a signal that originated as iZQCs during $t_1$. The evolution from this period is $(\omega_I - \omega_S) t_1$. The selective inversion pulse converts this signal into iDQC, which evolves during $\tau$ and acquired an evolution of $-(\omega_I + \omega_S) \star \tau$. The selective mixing pulse converts the iDQC into a two-spin iSQC and dipolar couplings convert this into detectable one-spin SQCs. The evolution before and after the refocusing pulse cancels out, and the total evolution is $2\omega_I \tau$. The total evolution for this signal is $-(\omega_I - \omega_S) \star (t_1 + \tau)$, an equal and opposite

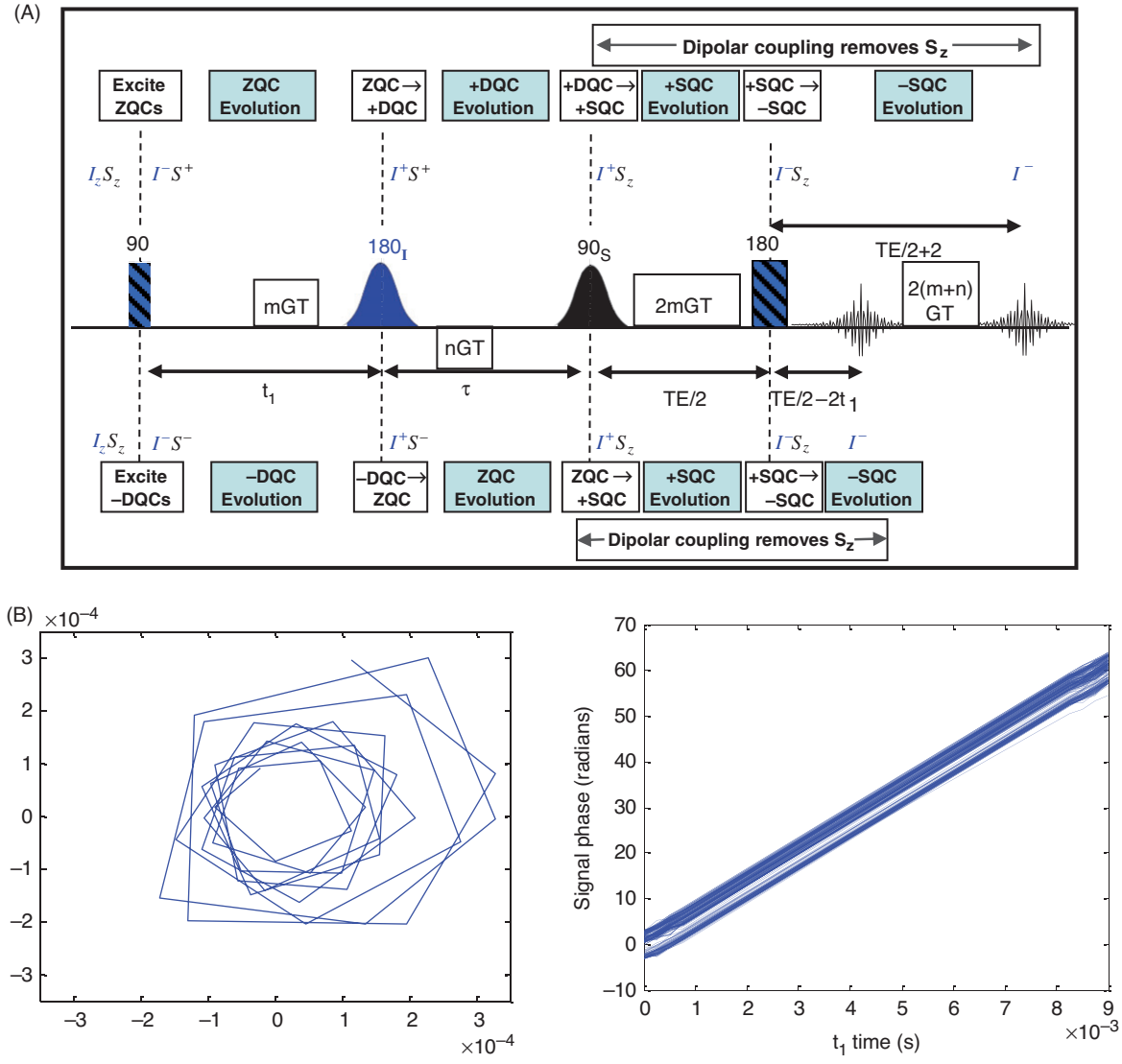


Figure 2. (A) HOT pulse sequence [32, 51]. The HOT sequence is used to detect temperatures using iMQCs. Two coherence pathways are preserved, in which the initial evolution is iDQC which is converted to iZQC, and the second is one in which the magnetisation is initially iZQC and is converted to iDQC. The separate pathways evolve for different amounts of time allowing for fast acquisition of iMQC temperatre maps. (B) Left: Representative signal evolution obtained during a HOT experiment. In this case, $t_1$ was incremented 48 times. As $t_1$ changes, the phase of the signal changes, and the rate of that change can be used to determine the iZQC frequency. In this figure, each vertex represents the acquisition of a $t_1$ increment, and the evolution of the phase of the signal is shown. Right: If the phase evolution shown on the left is unwrapped and plotted versus $t_1$ (time) the slope of the resulting line can be used to extract the iZQC frequency. The lines on the right show the phase for every pixel in an HOT temperature experiment. The slope of the line is determined using a linear least squares fitting of the $t_1$ time versus phase data points.

amount of evolution as the signal acquired in the first acquisition window.

In summary, the HOT pulse sequence works by suppressing the unwanted coherence pathways. The signal from unwanted temperature-insensitive same-spin iMQCs are not preserved by this sequence, and neither are the SQC coherences. The selective 180° pulse only converts the mixed spin coherences from iZQC to iDQC (and vice versa) and the gradients are designed to only allow those coherences to survive. The multiple acquisition windows acquires signal with different amounts of iMQC evolution, permitting acceleration of the temperature map and rapid iMQC temperature imaging.

## Results

### *Demonstration of the HOT sequence in phantoms*

The improvement in temperature detection using the HOT sequence was first demonstrated in phantoms. The first example of iMQC-based temperature

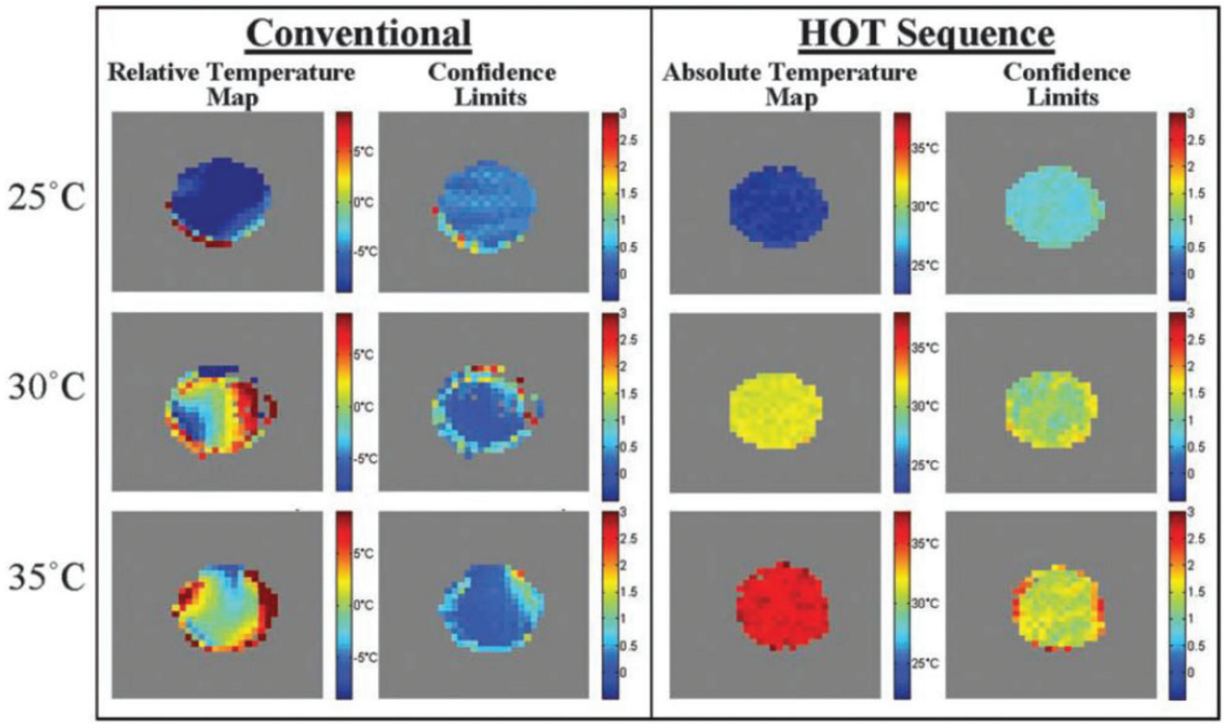


Figure 3. Demonstration of HOT sequence in cream phantom at three temperatures [32]. The conventional maps were taken by monitoring the changes in phase of the water signal in a phantom of cream (homogeneous mixture of water and fat) as the sample was heated. Large distortions in the detected temperature were observed (due both to shimming imperfections and to susceptibility gradients created during heating), complicating the temperature detection. The images collected using the HOT sequence show only one temperature across the images, demonstrating the clean temperature detection of the HOT sequence. Next to both sets of images are the 90% confidence intervals showing the quality of the fit of each voxel. TE (echo time) = 60 ms, TR (repetition time) = 5 s, $\tau = 2.67$ ms, $t_1 = 3$ to 11 ms, indirect spectral width = 5000 Hz, correlation distance = 140 μm, voxel size = 0.0625 $cm^3$.

detection is found in [32] (Figure 3). In this experiment a phantom of cream (homogeneous mixture of water and fat) was heated to three different temperatures and temperature images were taken using the HOT pulse sequence. In addition, standard proton frequency maps were taken directly after each HOT image. The images taken with the HOT sequence show a uniform temperature across the sample, and a standard deviation <1 Hz (which at 7T corresponds to 0.33°C). Next to both sets of temperature maps are figures showing the 90% confidence interval based on the quality of the fit of each voxel. While the standard PRF maps show large variations in the detected temperature (caused by susceptibility gradients) the HOT images show only the temperature dependence of the signal.

*Demonstration of the HOT sequence* in vivo

The demonstration of the ability of the HOT sequence to detect temperature *in vivo* was presented in [32]. In Figure 4A, an obese mouse (ob/ob, Jackson Laboratories) was imaged using the HOT sequence showing that this method can be used to detect temperature *in vivo*. Figure 4A shows the HOT temperature map superimposed on a standard anatomical spin echo image. The HOT image was ungated (respiratory) and acquired in 2 min. The image shows good uniformity in the temperature values of each pixel, which is expected in the natural body temperature of a mouse. The 2 min acquisition is sufficiently fast to allow for dynamic temperature mapping as shown in Figure 4B. In Figure 4B a mouse was heated by a warm tube of water running next to it, showing that the 2 min temporal resolution is sufficient to detect heating changes.

## Conclusions

The HOT sequence has been demonstrated in several papers [32, 51, 59] to provide clean, absolute temperature maps. This sequence is designed to work best in situations where there are comparable amounts of water and fat at the correlation distance, making it ideally suited for temperature imaging in high fat tissues. In addition, the HOT sequence

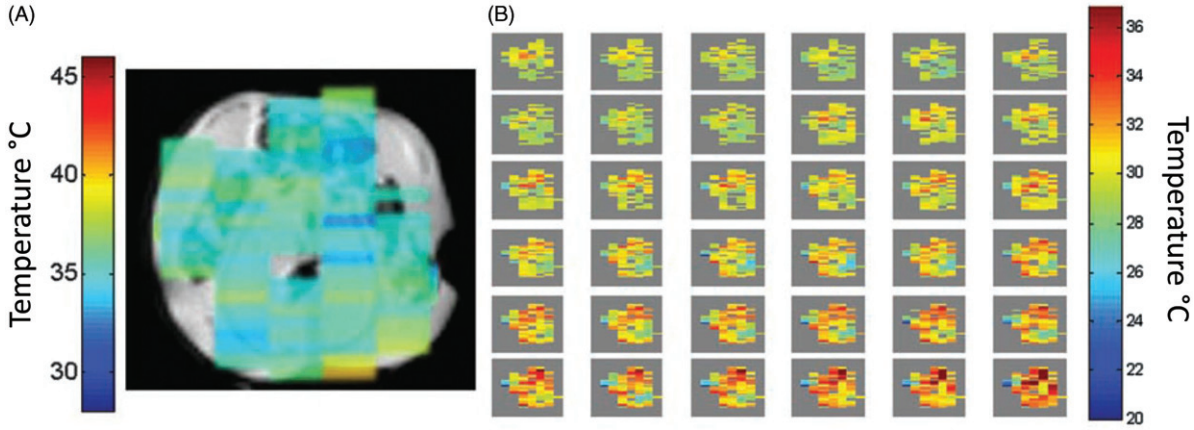


Figure 4. In vivo demonstration of the HOT sequence [32]. (A) shows the overlay of a 2-minute HOT temperature maps on an anatomical image of a mouse. The uniformity of the voxels is as expected for the natural temperature distribution of a mouse. (B) is of a mouse with a tube of water next to it. The water is heated over the course of the experiment and the heating is observed in the temperature images. TE = 40 ms, TR = 2 s, $\tau = 10.66$ ms, $t_1 = 3$–13 ms, indirect spectral width = 4000 Hz, correlation distance = 0.0945 mm, voxel size = 0.25 $cm^3$.

works well in regions with large susceptibility gradients, providing a useful tool for temperature detection in the breast or other tissue regions where susceptibility gradients play a large role.

One possible limitation of the sequence is the lower signal-to-noise ratio inherent in any iMQC experiment. While some advances have been made [60] to enhance the SNR of iMQC experiments, most standard experiments have about 10% of the SNR of a standard image. Since the HOT experiment includes more pulses than the standard CRAZED experiment it is more sensitive to flip angle and pulse imperfections, which can further reduce the signal intensity.

The frequency measured by the HOT sequence is the difference between the water signal and the fat signal. Since fat is made up of many different resonance frequencies, the detected HOT signal is a weighted average of the difference in resonance frequency between the water and the different fat components. Since different fats have different compositions, it is possible that the detected iMQC frequency might be slightly altered in different types of tissue. This can be corrected for by acquiring one image at a known temperature, and then the iMQC frequency for that tissue would be known.

One final concern for use of this sequence in vivo is the distribution of water and fat in the tissue of interest. The HOT sequence relies on water and fat spins that are in the same environment. If the water or fat in a tissue is highly compartmentalised, then the HOT sequence would only be able to detect temperature at the interfaces of the compartments, further reducing the signal of the sequence.

Accurate detection of temperature in tissues with high fat content (such as the breast) allows for the use of hyperthermic treatments in breast tissue. While standard PRF methods in the breast have been used [3, 61, 62], the fundamental problem of large susceptibility changes from the fat makes this type of technique difficult. Other approaches have been taken, such as monitoring changes in the spin density, changes in relaxation rate $T_1$ and diffusion [63–71] but their temperature dependence is tissue-type dependent and signal changes are induced by coagulation. Methods based on intermolecular multiple quantum coherences such as the HOT method provide the opportunity to detect temperature accurately and on an absolute scale, without complications from changes in susceptibility with heating as well as magnetic field drift and inhomogeneities.

***Declaration of interest:*** This work was funded by NIH grant EB 2122. The authors alone are responsible for the content and writing of the paper.

## References

1. Wust P, Hildebrandt B, Sreenivasa G, Rau B, Gellermann J, Riess H, Felix R, Schlag PM. Hyperthermia in combined treatment of cancer. Lancet Oncol 2002;3:487–497.
2. Falk MH, Issels RD. Hyperthermia in oncology. Int J Hyperthermia 2001;17:1–18.
3. Furusawa H, Namba K, Thomsen S, Akiyama F, Bendet A, Tanaka C, Yasuda Y, Nakahara H. Magnetic resonance-guided focused ultrasound surgery of breast cancer: Reliability and effectiveness. J Am Coll Surg 2006;23:54–63.
4. Mirza AN, Fornage BD, Sneige N, Kuerer HM, Newman LA, Ames FC, Singletary E. Radiofrequency ablation of solid tumors. Cancer J 2001;7:95–95.
5. Kim JH, Hahn EW. Clinical and biological studies of localized hyperthermia. Cancer Res 1979;39:2258–2261.

6. Vujaskovic Z, Dewhirst M, Jones E, Thrall D. Re-setting the biologic rationale for thermal therapy. Int J Hyperthermia 2005;21:779–790.
7. Jones E, Thrall D, Dewhirst MW, Vujaskovic Z. Prospective thermal dosimetry: The key to hyperthermia's future. Int J Hyperthermia 2006;22:247–253.
8. Jones EL, Oleson JR, Prosnitz LR, Samulski TV, Vujaskovic Z, Yu DH, Sanders LL, Dewhirst MW. Randomized trial of hyperthermia and radiation for superficial tumors. J Clin Oncol 2005;23:3079–3085.
9. Hand JW, Machin D, Vernon CC, Whaley JB. Analysis of thermal parameters obtained during phase III trials of hyperthermia as an adjunct to radiotherapy in the treatment of breast carcinoma. Int J Hyperthermia 1997;13:343–364.
10. Kapp DS, Cox RS. Thermal treatment parameters are most predictive of outcome in patients with single tumor nodules per treatment field in recurrent adenocarcinoma of the breast. Int J Radiat Oncol Biol Phys 1995;33:887–899.
11. Oleson JR, Samulski TV, Leopold KA, Clegg ST, Dewhirst MW, Dodge RK, George SL. Sensitivity of hyperthermia trial outcomes to temperature and time – Implications for thermal goals of treatment. Int J Radiat Oncol Biol Phys 1993;25:289–297.
12. Seegenschmiedt MH, Martus P, Fietkau R, Iro H, Brady LW, Sauer R. Multivariate analysis of prognostic parameters using interstitial thermoradiotherapy (IHT-IRT) – tumor and treatment variables predict outcome. Int J Radiat Oncol Biol Phys 1994;29:1049–1063.
13. Sherar M, Liu FF, Pintilie M, Levin W, Hunt J, Hill R, Hand J, Vernon C, vanRhoon G, vanderZee J, et al. Relationship between thermal dose and outcome in thermoradiotherapy treatments for superficial recurrences of breast cancer: Data from a phase III trial. Int J Radiat Oncol Biol Phys 1997;39:371–380.
14. Vujaskovic Z, Kim D, Jones E, Lan L, McCall L, Dewhirst M, Craciunescu O, Stauffer P, Liotcheva V, Betof A, et al. A phase I/II study of neoadjuvant liposomal doxorubicin, paclitaxel, and hyperthermia in locally advanced breast cancer. Int J Hyperthermia 2010; submitted.
15. Carter DL, MacFall JR, Clegg ST, Wan X, Prescott DM, Charles HC, Samulski TV. Magnetic resonance thermometry during hyperthermia for human high-grade sarcoma. Int J Radiat Oncol Biol Phys 1998;40:815–822.
16. Clegg ST, Das SK, Zhang Y, Macfall J, Fullar E, Samulski TV. Verification of a hyperthermia model method using MR thermometry. Int J Hyperthermia 1995;11:409–424.
17. Craciunescua OI, Stauffer PR, Soher BJ, Wyatt CR, Arabe O, Maccarini P, Das SK, Cheng KS, Wong TZ, Jones EL, et al. Accuracy of real time noninvasive temperature measurements using magnetic resonance thermal imaging in patients treated for high grade extremity soft tissue sarcomas. Med Phys 2009;36:4848–4858.
18. Depoorter J. Noninvasive MRI thermometry with the proton-resonance frequency method: Study of susceptibility effects. Magn Reson Med 1995;34:359–367.
19. Depoorter J, Dewagter C, Dedeene Y, Thomsen C, Stahlberg F, Achten E. Noninvasive MRT thermometry with the proton-resonance frequency (PRF) method – In vivo results in human muscle. Magn Reson Med 1995;33:74–81.
20. Gellermann JW, Feussner W, Fähling A, Nadobny H, Hildebrandt B, Felix R, Wust P. Methods and potentials of magnetic resonance imaging for monitoring radiofrequency hyperthermia in a hybrid system. Int J Hyperthermia 2005;21.
21. Ishihara Y, Calderon A, Watanabe H, Okamoto K, Suzuki Y, Kuroda K, Suzuki Y. Precise and fast temperature mapping using water proton chemical-shift. Magn Reson Med 1995;34:814–823.
22. Rieke V, Pauly KB. MR thermometry. J Magn Reson Imag 2008;27:376–390.
23. Samulski TV, Clegg ST, Das S, Macfall J, Prescott DM. Application of a new technology in clinical hyperthermia. Int J Hyperthermia 1994;10:389–394.
24. Hindman JC. Proton resonance shift of water in the gas and liquid states. J Chem Phys 1966;44:4582–4592.
25. Abragam A. Principles of nuclear magnetism. Oxford: Oxford University Press; 1961.
26. McDannold N. Quantitative MRI-based temperature mapping based on the proton resonant frequency shift: Review of validation studies. Int J Hyperthermia 2005;21:533–546.
27. Schenck JF. The role of magnetic susceptibility in magnetic resonance imaging: MRI magnetic compatibility of the first and second kinds. Med Phys 1996;23:815–850.
28. Chu SCK, Xu Y, Balschi JA, Springer CS. Bulk magnetic susceptibility shifts in NMR studies of compartmentalized samples: Use of paramagnetic reagents. Magn Reson Med 1990;13:239–262.
29. Dickinson WC. The time average magnetic field at the nucleus in nuclear magnetic resonance experiments. Phys Rev 1951;81:717–731.
30. Sprinkhuizen S, Konings M, Bakker C, Bartels L. Heating of fat leads to significant temperature errors in PRFS-based MR thermometry. Proceedings of the 17th Scientific Meeting, International Society for Magnetic Resonance in Medicine, Honolulu, 2009, p 2532.
31. Stollberger R, Ascher PW, Huber D, Renhart W, Radner H, Ebner F. Temperature monitoring of interstitial thermal tissue coagulation using MR phase images. J Magn Reson Imaging 1998;8:188–196.
32. Galiana G, Branca RT, Jenista ER, Warren WS. Accurate temperature imaging based on intermolecular coherences in magnetic resonance. Science 2008;322:421–424.
33. Ahn S, Lisitza N, Warren WS. Intermolecular zero-quantum coherences of multi-component spin systems in solution NMR. J Magn Reson 1998;133:266–272.
34. Ahn S, Warren WS. of intermolecular dipolar couplings in solution NMR in separated time intervals: The competition for coherence transfer pathways. Chem Phys Lett 1998;291:121–129.
35. Ahn S, Warren WS, Lee S. Quantum treatment of intermolecular multiple-quantum coherences with intramolecular J coupling in solution NMR. J Magn Reson 1997;128:114–129.
36. Bouchard LS, Warren WS. Multiple-quantum vector field imaging by magnetic resonance. J Magn Reson 2005;177:9–21.
37. Bowtell R. Indirect detection via the dipolar demagnetizing field. J Magn Reson 1992;100:1–17.
38. Branca RT, Silvia C, Bruno M. About the CRAZED sequence. Concepts Magn Reson 2004;21A:22–36.
39. Cho JH, Ahn S, Lee C, Hong KS, Chung KC, Chang SK, Cheong C, Warren WS. Magnetic resonance microscopic imaging based on high-order intermolecular multiple-quantum coherences. Magn Reson Imaging 2007;25:626–633.
40. He QH, Richter W, Vathyam S, Warren WS. Intermolecular multiple-quantum coherences and cross correlations in solution nuclear-magnetic-resonance. J Chem Phys 1993;98:6779–6800.
41. Lee S, Richter W, Vathyam S, Warren WS. Quantum treatment of the effects of dipole-dipole interactions in liquid nuclear magnetic resonance. J Chem Phys 1996;105:874–900.
42. Lin YY, Ahn S, Murali N, Brey W, Bowers CR, Warren WS. High-resolution, >1 GHz NMR in unstable magnetic fields. Phys Rev Lett 2000;85:3732–3735.

43. Richter W, Warren WS. Intermolecular multiple quantum coherences in liquids. Concepts Magn Reson 2000;12:396–409.
44. Richter W, Lee SH, Warren WS, He QH. Imaging with intermolecular multiple-quantum coherences in solution nuclear-magnetic-resonance. Science 1995;267:654–657.
45. Rizi RR, Ahn S, Alsop DC, Garrett-Roe S, Mescher M, Richter W, Schnall MD, Leigh JS, Warren WS. Intermolecular zero-quantum coherence imaging of the human brain. Magn Reson Med 2000;43:627–632.
46. Vathyam S, Lee S, Warren WS. Homogeneous NMR spectra in inhomogeneous fields. Science 1996;272:92–96.
47. Warren WS, Lee S, Richter W, Vathyam S. Correcting the classical dipolar demagnetizing field in solution NMR. Chem Phys Lett 1995;247:207–214.
48. Warren WS. Rethinking solution NMR. Science 1998;280:398–399.
49. Warren WS, Ahn S, Mescher M, Garwood M, Ugurbil K, Richter W, Rizi RR, Hopkins J, Leigh JS. MR imaging contrast enhancement based on intermolecular zero quantum coherences. Science 1998;281:247–251.
50. Warren WS, Richter W, Andreotti AH, Farmer BT. Generation of impossible cross-peaks between bulk water and biomolecules in solution NMR. Science 1993;262:2005–2009.
51. Jenista ER, Galiana G, Branca RT, Yarmolenko PS, Stokes AM, Dewhirst MW, Warren WS. Application of mixed spin iMQCs for temperature and chemical-selective imaging. J Magn Reson 2010; accepted.
52. Balla DZ, Melkus G, Faber C. Spatially localized intermolecular zero-quantum coherence spectroscopy for in vivo applications. Magn Reson Med 2006;56:745–753.
53. Chen X, Lin MJ, Chen Z, Zhong JH. Fast acquisition scheme for achieving high-resolution MRS with J-scaling under inhomogeneous fields. Magn Reson Med 2009;61:775–784.
54. Frydman L, Lupulescu A, Scherf T. Principles and features of single-scan two-dimensional NMR spectroscopy. J Am Chem Soc 2003;125:9204–9217.
55. Frydman L, Scherf T, Lupulescu A. The acquisition of multidimensional NMR spectra within a single scan. Proc Natl Acad Sci USA 2002;99:15858–15862.
56. Galiana G, Branca RT, Warren WS. Ultrafast intermolecular zero quantum spectroscopy. J Am Chem Soc 2005;127:17574–17575.
57. Jianhui Z, Edmund K, Zhong C. fMRI of auditory stimulation with intermolecular double-quantum coherences (iDQCs) at 1.5T. Magn Reson Med 2001;45:356–364.
58. Schneider JT, Faber C. BOLD imaging in the mouse brain using a TurboCRAZED sequence at high magnetic fields. Magn Reson Med 2008;60:850–859.
59. Branca RT, Warren WS. In vivo brown adipose tissue detection and characterization using water-lipid intermolecular zero quantum coherences. Magn Reson Med 2010; submitted.
60. Branca RT, Galiana G, Warren WS. Enhanced nonlinear magnetic resonance signals via square wave dipolar fields. J Chem Phys 2008;129.
61. Hynynen K, Pomeroy O, Smith DN, Huber PE, McDannold NJ, Kettenbach J, Baum J, Singer S, Jolesz FA. MR imaging-guided focused ultrasound surgery of fibroadenomas in the breast: A feasibility study. Radiology 2001;219:176–185.
62. Kohler MO, Mougenot C, Quesson B, Enholm J, Le BailB, Laurent C, Moonen CTW, Ehnholm GJ. Volumetric HIFU ablation under 3D guidance of rapid MRI thermometry. Med Phys 2009;36:3521–3535.
63. Bleier AR, Jolesz FA, Cohen MS, Weisskoff RM, Dalcanton JJ, Higuchi N, Feinberg DA, Rosen BR, McKinstry RC, Hushek SG. Real-time magnetic resonance imaging of laser heat deposition in tissue. Magn Reson Med 1991;21:132–137.
64. Bottomley PA, Foster TH, Argersinger RE, Pfeifer LM. A review of normal tissue hydrogen NMR relaxation times and relaxation mechanisms from 1–100 MHz: Dependence on tissue type, NMR frequency, temperature, species, excision, and age. Med Phys 1984;11:425–448.
65. Cady EB, Dsouza PC, Penrice J, Lorek A. The estimation of local brain temperature by in-vivo H-1 magnetic resonance spectroscopy. Magn Reson Med 1995;33:862–867.
66. Hynynen K, McDannold N, Mulkern RV, Jolesz FA. Temperature monitoring in fat with MRI. Magn Reson Med 2000;43:901–904.
67. Kuroda K, Oshio K, Chung AH, Hynynen K, Jolesz FA. Temperature mapping using the water proton chemical shift: A chemical shift selective phase mapping method. Magn Reson Med 1997;38:845–851.
68. Lewa CJ, Majewska Z. Temperature relationships of proton spin-lattice relaxation time – T1 in biological tissues. Bull Cancer (Montrouge) 1980;67:525–530.
69. Marshall I, Karaszewski B, Wardlaw JM, Cvoro V, Wartolowska K, Armitage PA, Carpenter T, Bastin ME, Farrall A, Haga K. Measurement of regional brain temperature using proton spectroscopic imaging: Validation and application to acute ischemic stroke. Magn Reson Imaging 2006;24:699–706.
70. Morvan D, Leroywillig A, Malgouyres A, Cuenod CA, Jehenson P, Syrota A. Simultaneous temperature and regional blood-volume measurements in human muscle using an MRI fast diffusion technique. Magn Reson Med 1993;29:371–377.
71. Parker DL, Smith V, Sheldon P, Crooks LE, Fussell L. Temperature distribution measurements in two-dimensional NMR imaging. Med Phys 1983;10:321–325.